Nanotechnology **17** (2006) 2722–2729 doi:10.1088/0957-4484/17/11/002

Interdigitated 50 nm Ti electrode arrays fabricated using XeF_2 enhanced focused ion beam etching

Ch Santschi[1,2], M Jenke[2], P Hoffmann[2] and J Brugger[1]

[1] Laboratoire de Microsystèmes (LMIS), Station 17, CH1015 Lausanne, Switzerland
[2] Laboratoire d'Optique Appliquée (LOA), École Polytechnique Fédérale de Lausanne, Station 17, CH1015 Lausanne, Switzerland

E-mail: Juergen.Brugger@epfl.ch

Received 1 November 2005, in final form 5 April 2006
Published 16 May 2006
Online at stacks.iop.org/Nano/17/2722

Abstract
The fabrication of interdigitated titanium nanoelectrode arrays of 50 nm in width and spacing is described in this work. The nanoarrays have been realized using a Ga^+ focused ion beam (FIB). FIB milling is typically accompanied by redeposition of removed material, which represents an important hindrance for milling closely spaced nanostructures. Redeposition effects have been reduced by means of XeF_2 gas assistance, which increases the etch yield by a factor of seven compared with pure ion milling. Furthermore, we used a simple adsorption model, which led to the conclusion that dwell time and refresh time should be <500 ns and >30 ms, respectively, for optimized XeF_2 assisted Ti milling. The measured resistance R of the electrodes is higher than 1 GΩ.

1. Introduction

The progress in fabrication methods for nanostructures made in the last few years opens the door for new applications in fields such as biotechnology [1] and microelectrochemistry [2–4], as well as microelectronics [5]. Interdigitated electrode arrays (IEAs) of micrometric dimensions and nanometric gaps and widths offer various advantages compared to micrometric IEAs. Applications for nano-IEAs are, for instance, impedance spectroscopy of biomolecules [6], DNA biosensors [7, 8], and gas sensors [9]. In the domain of sensors, handling of small amounts of the substances under test and on-chip solutions including various functions such as mixing, heating, and *in situ* detection is desirable and becomes feasible using nanoscale IEAs. The generation of strong and localized electrical fields is very useful, for example, to change the dipole orientation of molecules or diffusion of ions in a solution in the sphere of very small volumes. Such strong electrical fields constrict, for instance, the rotational motion of dipoles in solution, which manifest itself by a gradual decrease of the electric permittivity, which is proportional to the square of the field strength [10]. Such high electrical field strength may be achieved using interdigitated nanoelectrodes. Thus, there is a considerable interest in fabrication methods for nanoscale IEAs.

Despite the overall recent progress in nanofabrication technology, the realization of arrayed nanoscale electrode is still challenging, especially in the sub-100 nm range. Pairs of nanometric electrodes were recently fabricated by Nagase *et al* [11]. Two electrodes were engraved in a 10–30 nm thick gold layer covering an oxidized Si substrate employing focused ion beam (FIB) techniques. Electrode pairs of similar size have also been produced by Zandbergen [12]. They modified a free-standing gold layer using a highly focused electron beam obtained in a transmission electron microscope (TEM). This permits *in situ* observation of the fabrication process and therefore a very precise control of the feature size. Arrays of vertically aligned electrodes with a few tens of nanometres width have been realized with a bottom-up approach using carbon nanotubes [3, 4]. Furthermore, nanoscale IEAs have been fabricated by Montelius [6] using electron beam lithography (EBL) and the lift-off technique. These structures were realized in 20 nm Au and eutectic Au/Ge layers that are evaporated onto a wet oxidized SiO_2. They achieved arrays with electrode spacing down to 150 nm. Nanoimprint (NIL) and UV lithography (UVL) are further potential nanostructuring methods. Applying these techniques IEAs with down to 100 nm separation between electrodes

 © 2006 IOP Publishing Ltd Printed in the UK

have been realized [13]. IEAs of 400 nm width and 200 nm spacing have been produced by Schift [14] using hot embossing lithography (HEL). An original method of realization of nanoscale IEAs has been presented by Van Gerwen *et al* [15]. They took advantage of the properties of directional evaporation under vacuum conditions. A substrate is particularly moulded in the way that IEAs are formed by the evaporation process due to shadow effects. With this low-cost fabrication method sub-micrometre IEAs have been realized.

The techniques mentioned above describe sundry fabrication methods, which permit either the realization of small electrode pairs down to 20 nm or IEAs with feature sizes down to hundreds of nanometres. In this work we show that FIB gas assisted etching is a possible method to realize IEAs with electrode width and spacing down to a few tens of nanometres. Furthermore, we demonstrate that ion induced etching leads to a significant improvement of the quality of closely spaced nanofeatures compared to the pure FIB milling technique, whereas individual isolated nanostructuring is feasible using the standard FIB technique.

Ion beam induced chemical reactions allow the material to be volatilized locally and pumped away. This leads to an enhanced milling rate but also reduces redeposition effects [16–18]. The use of XeF_2 gas has been successful for different materials such as diamond [19], Si, SiO_2, and W [17], because the generated fluorides of this materials are volatile. The possibility of gas assisted etching of titanium (Ti) using an e-beam and XeF_2 was also shown by DeMarco *et al* [20]. Since Ti is a biocompatible material it is used in many biotechnological applications.

In this work we use ion induced etching with XeF_2 in order to reduce material redeposition during Ti removal, and hence to improve the final quality of the nanostructures. Moreover, we have experimentally quantified the etch rate enhancement for the XeF_2/Ti system. For a better interpretation of the obtained experimental results a simple adsorption model [21–24] has been applied. Additionally, the realized IEAs have been tested for electrical insulation by V–I measurements.

2. Experimental set-up

2.1. Focused ion beam

FIB systems are used in a wide range of applications such as imaging [25], beam induced deposition [26], doping of semiconducting and other materials [27], ion beam lithography [28], and physical sputtering of material by ion impact for micro- and nanopatterning, which is one of the principal applications [29, 30]. For our experiments we used a dual beam Nova 600 NanoLab instrument from FEI Company, which works with a Ga^+ ion beam. The principle of a dual beam system is described in detail elsewhere [31]. In order to have a small beam diameter and reasonably short milling durations the experiments have been carried out with an ion acceleration voltage and current set to $U_i = 30$ kV and $I_i = 10$ pA, respectively, which results in a nominal beam diameter d_b of 12 nm (full width at half maximum, FWHM).

The beams of the Nova 600 NanoLab are pixel controlled, which allows the pattern to be defined in different ways, such as direct drawing of the patterns composed of a given set of basic patterns, individual control of pixels (stream files), or bitmap files (bmp). In our experiments the patterns have been defined using bmps. Figure 1 displays the bmp pattern used for the interdigitated electrodes. The patterning proceeding is a precise pixel-by-pixel movement, where for black and white pixels the ion beam is blanked and not blanked, respectively. The pixel density ρ_p of the bmp is calculated according to equation (1) based on the beam diameter d_b, and the desired overlap, which is 50% in our experiments:

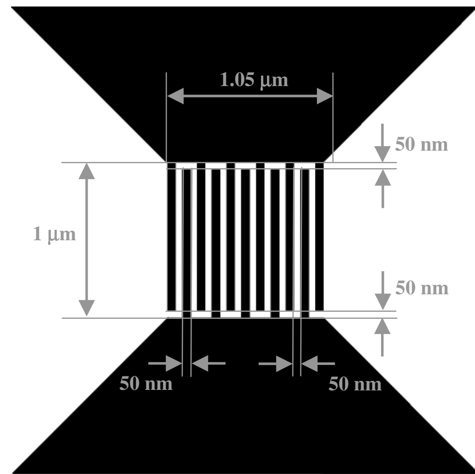

Figure 1. Drawing of the bitmap file used for FIB milling. Pixels lying in the white regions are exposed to the FIB.

$$\rho_p = \frac{1\ \mu\text{m} \times 100}{d_b \text{ overlap}}. \quad (1)$$

Equation (1) leads to $\rho_p = 167$ pixel μm^{-1} for $d_b = 12$ nm.

The total ion dose D depends on the ion current I_i, the dwell time t_d, the number of white pixels n_w, and scans or passes p according to equation (2),

$$D = \frac{n_w t_d p}{A} I_i \quad (2)$$

where A represents the total area of the milled pattern and the duration that the beam is pointing to an individual target pixel is named the dwell time t_d. The number of pixels n_w may be achieved using ρ_p and the geometrical dimensions of the bmp pattern.

The sputtering rate R is a useful quantity in order to estimate the running time of a removal process. R is given according to equation (3),

$$R = \frac{V}{Q} = \frac{V}{I_i t} \quad (3)$$

where V, Q and t are the volume of the removed material, the required charge or number of Ga^+ and the milling time, respectively.

Furthermore, gas assisted milling using XeF_2 can be performed using FIB tools. The gas flow F is controlled by the precursor temperature $T_p = 28\,^\circ$C (given for this instrument) and has been estimated using the mass of XeF_2 in the filled reservoir, the lifetime of a filling and the geometrical

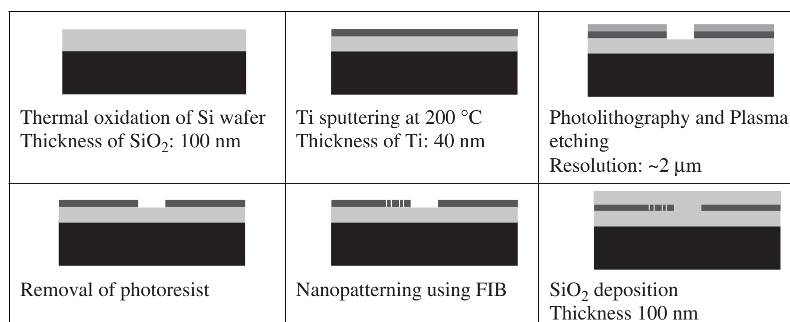

Figure 2. Process flow used for the fabrication of the embedded nanoelectrode array.

dimensions of the needle [32]. This leads to the following equation (4):

$$F(\mathrm{XeF_2}) = \frac{\rho V_r}{M_A} N_A \frac{4}{t d_N^2 \pi} \tag{4}$$

$\rho = 4.3$ g cm^{-3} is the density of XeF_2 [33]; $V_r = 5$ cm^{-3} is the reservoir volume; $M_A = 169.3$ g mol^{-1} is the atomic weight of XeF_2 [33]; N_A is the Avogadro's number; $t = 80$ h is the lifetime of one filling; $d_N = 500$ μm is the needle diameter.

Using this approach leads to a flow of $F = 1.3 \times 10^{20}$ molecule s^{-1} cm^{-2} at the outlet of the needle. The gas distribution between needle and substrate were calculated with Monte Carlo simulations. According to this simulation, using the geometry of our set-up, the gas flow is ca. 50% of F at the position of the ion–substrate interaction [34].

Finally, measurements of the sputtering yields have revealed a dependence on the incident angle of the ions [35]. We performed all milling processes with an angle of 90°, i.e. perpendicular incidence.

2.2. Electrical measurements

The electrode arrays have been tested on their electrical Insulation, performing two-point V–I-measurements using an HP 4156A semiconductor parameter analyser. The measurements were performed in a measurement station in the dark in order to avoid photon induced conduction due to the p-doped Si wafer and possible Ga^+ doping. V–I measurements were carried out before and after embedding the electrodes in SiO_2.

3. Sample preparation

Prior to carrying out FIB operations the substrates were prestructured by standard photolithography in order to add bonding pads to the nanoelectrodes. The processing steps are schematically presented in figure 2. A Ti layer was superimposed onto a doped Si test-wafer covered with a 100 nm SiO_2 layer, produced by a dry oxidation process, prior to the photolithography process followed by a dry etch step with BCl_3. This superjacent Ti layer has been deposited by a sputtering process at temperature $\vartheta = 200\,°$C, a chamber pressure of 3×10^{-8} mbar, and a sputtering rate of 75 nm min^{-1} using a Spider 600 instrument (Pfeiffer Vacuum). The thickness d_s of the Ti layer was 40 nm measured using an atomic force microscope AFM (Topometrix Explorer, Veeco). The resistivity of the Si wafer is indicated to be in the range of 0.1–100 Ω cm.

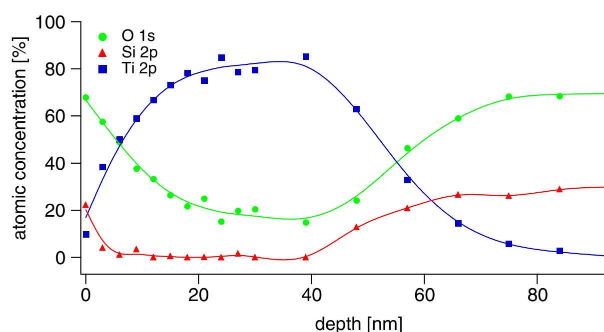

Figure 3. Depth profile of the relative atomic concentrations of Ti (2p), O (1s) and Si (2p) obtained by x-ray photoelectron spectroscopy (XPS). The depth values are obtained from the known thickness of the Ti layer (40 nm) and the sputter times of the Ar^+ ion gun, assuming constant etch rates for the different compounds. The corresponding measurements have been carried out at 454.2–458.9 eV, 531.4–532.7 eV and 96.2–105 eV for Ti, O and Si, respectively.

(This figure is in colour only in the electronic version)

An XPS analysis of the Ti layers revealed the presence of oxygen in the sputtered Ti layer. The origin of this contamination is not clear. Figure 3 displays the relative concentration of Ti, O and Si as a function of the layer depth.

The pattern of the prestructures is shown in figure 4, consisting of a 2×2 μm^2 area in the centre of the structure where FIB milling is carried out and two contact pads for electrical measurements.

After engraving of the nanostructures using the FIB technique the structures have been coated with sputtered SiO_2 in order to realize embedded nanoelectrodes. The contact pads were covered using a Kepton tape prior to the accomplishment of SiO_2 coating in order to keep them uncovered for subsequent bonding. The sputtering process for SiO_2 was performed in a Spider 600 instrument in the presence of 10^{-4} mbar of oxygen in order to increase the quality of the SiO_2 layer.

4. Experiments and discussion

4.1. Nanoelectrode fabrication

For the fabrication of nanostructures the ion beam quality is of crucial importance. The requested quality is achieved adjusting focus and stigmatism very carefully. Subsequent to a rough adjustment on an adapted surface feature, nanoholes

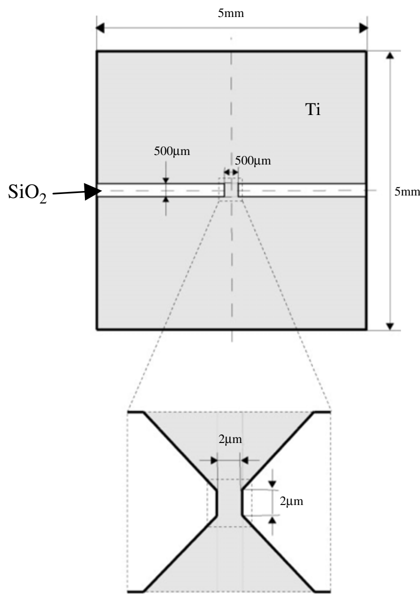

Figure 4. Ti prestructure fabricated with standard photolithography. The pattern consists of an area of $2 \times 2\ \mu m^2$ and two pads used for electrical contacts. The grey area is covered with Ti, whereas on the white area the underlying SiO_2 appears since the Ti has been removed using a dry etch process.

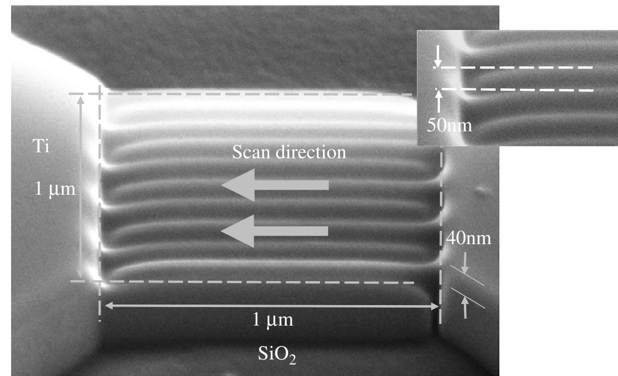

Figure 5. SEM image of interdigitated nanoelectrodes of 50 nm width, 50 nm gap and 40 nm thickness which have been produced using FIB without gas enhanced etching. The parameters are $I_i = 10$ pA, $U_i = 30$ kV, $t_d = 250$ ns and $p = 10 \times 10^3$ passes. The sample is tilted to 52°.

and squares with a diameter of a few hundred nanometres have been milled into the substrate in order to check the proper adjustment of focus and stigmatism. Analysing the milled test-structures thoroughly, slight distortions were observed due to surface charging, although the Ti structures and the underlying Si substrate were well grounded using a Cu tape covered with conducting glue. An efficient charge neutralization can be obtained by additional use of the e-beam whilst milling the nanostructures. An electron current, which is generated by the e-beam and on the order of 10 times higher than the ion current, leads to a good discharging of the substrate and solved this problem. For the e-beam the acceleration voltage was set to $U_e = 10$ kV and the current to $I_e = 130$ pA, and a dwell time t_d of 1 μs was used in combination with an ion current $I_i = 10$ pA. The resolution of the e-beam image and the horizontal field width (HFW) have been set to 512×422 pixels and 5.12 μm, respectively. The set HFW corresponds to a magnification of 25 000.

4.1.1. Milling without gas-enhanced etching. Prior to the array fabrication single slits of 50 nm in width and 1000 nm in length have been successfully engraved in the Ti layer, which confirms the good quality of the ion beam. Subsequently, the interdigitated electrodes were milled without gas-enhanced etching using the beam parameters mentioned above. Furthermore, the dwell time t_d and the number of passes p have been set to 250 ns and 10×10^3, respectively. The dwell time has been kept short because working with short t_d and large p leads to better results than vice versa. Figure 5 displays an SEM image of the $1 \times 1\ \mu m^2$ electrode array. The ion beam has been steered in raster mode, which means the scan direction is from right to left starting at the bottom with respect to figure 5. Analysing the SEM image a non-uniform milling depth of the pattern may be observed. Patterns with small sizes and close spacing suffer a reduction of sputtering rate, which may be attributed to redeposition; thus, the milling rate depends on the size and the spacing of the pattern. Furthermore, the structures between the electrodes are deeper on the left-hand side of the pattern, where the beam ends a single line-scan, which is also an effect of redeposition. Based on these observations we conclude that the fabrication of single 50 nm slits in a 40 nm Ti layer using FIB milling is feasible using the standard technique, though the fabrication of closely spaced structures is more challenging. One of the major problems for closely spaced nanostructures is redeposition, which affects adjacent structures milled before.

4.1.2. Milling with gas-assisted etching. The effects of redeposition can be counteracted by local introduction of reactive gases during the milling process. Figure 6 displays interdigitated Ti nanoelectrodes milled in a prestructured sample prepared as described above. They were fabricated by FIB chemical enhanced etching with XeF_2. As may be seen in figure 6, the electrodes have well defined edges, which is possible only with very low redeposition. The milling process has been carried out with an overlap, I_i, and U_i as mentioned above. Furthermore, the number of passes $p = 360$, $t_d = 500$ ns, $A = 0.53\ \mu m^2$, and $n_w = 14.6 \times 10^3$ lead to a dose $D = 5$ mC cm^{-2} according to equation (2). Using these parameters and the depth $d_s = 40$ nm of the structure the sputtering rate $R = 0.8\ \mu m^3$ nC^{-1} may be calculated according to equation (3). The delay between two subsequent passes, the refresh time t_r, is 128 ms. The refresh time t_r depends on t_d and the number of pixels n as will be discussed below.

The e-beam current I_e used for charge neutralization was changed in the range of $I_e = 33$ pA and $I_e = 540$ pA in order to examine its influence on the milling process, but it turned out that the contribution of the electron beam may be neglected compared to ion induced etching. This means the e-beam may also be used for charge neutralization in combination with ion induced chemical etching.

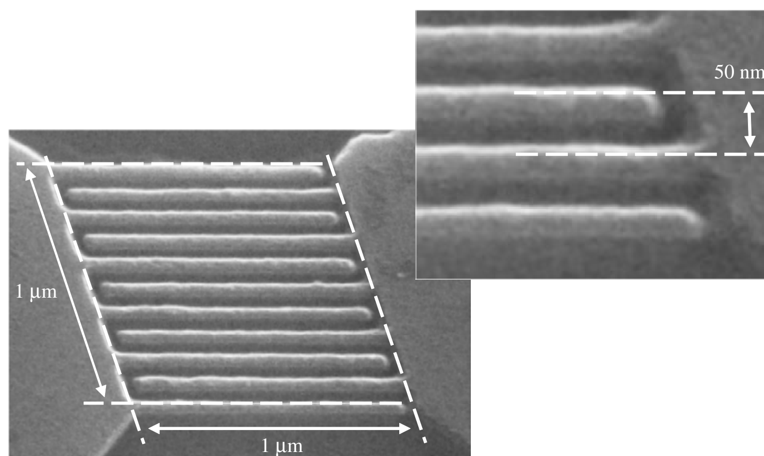

Figure 6. SEM image of interdigitated nanoelectrodes of 50 nm width, 50 nm gap, and 40 nm thickness. The electrodes have been fabricated using gas enhanced etching with XeF_2. The parameters are $I_i = 10$ pA, $U_i = 30$ kV, $t_d = 500$ ns, and $p = 360$ passes. The sample is tilted to 46°.

4.2. Sputtering rate

The ion induced etching process is a competition between precursor adsorption and desorption as well as ion induced decomposition with subsequent chemical reaction. The adsorption of the precursor starts with opening the valve of the gas inlet and continuously occurs, whereas the ion induced decomposition only takes place during t_d, in the presence of I_i. The time between two subsequent etch events on the same pixel is called refresh time t_r and is, together with t_d, one of the important parameters in this interplay.

In order to determine the optimal refresh time for the Ti/XeF_2 system the sputtering rate R was measured as a function of t_r with constant t_d and overlap. This was carried out by milling square structures of 1 μm length and 500 nm width into a Ti block with known ion doses and subsequent measurement of the removed volume. The volume is proportional to the depth of the square structures and has been measured *in situ* with an accuracy of ±10% by SEM imaging. t_r is composed of the scanning time t_s of one pass and an additional introduced waiting time t_w while the beam is blanked. Keeping the same width and length of the square structures requires constant t_s, and therefore t_r was varied, adapting t_w. The structures were milled with $t_d = 500$ ns, I_i and U_i as mentioned above and the magnification as well as the position of the gas needle were the same for all experiments. Measurements of the sputtering rate R without XeF_2 lead to a value $R = 0.11$ μm^3 nC^{-1}, whereas in the presence of XeF_2 the sputtering rate increases to $R_{ass} = 0.8$ μm^3 nC^{-1} for a refresh time $t_r > 50$ ms. This corresponds to an enhancement of the sputtering rate of a factor of seven or so, which is at the lower limit of the range of values reported for the Si/XeF_2, W/XeF_2 and SiO_2/XeF_2 systems. The values for these systems are 7–12 [17]. Figure 7 displays the sputtering rate R plotted as a function of t_r. The measured values are represented by dots. In further experiments R was determined varying t_d with constant refresh time $t_r = 150$ ms. The obtained rates are displayed as dots in figure 8. The physical sputtering rate R_p, which means in the absence of XeF_2, is given in earlier work by $R_p = 0.37$ μm^3 nC^{-1} [36]. The effective material removal is governed by sputtering and removal processes. Redeposition depends upon how the milling is performed. Using large numbers of passes p combined with short t_d also removes material already redeposited and thus leads to a reduction of the net amount of removed material. This may explain the difference in the sputtering rate R_p we obtained compared to the value found in the literature.

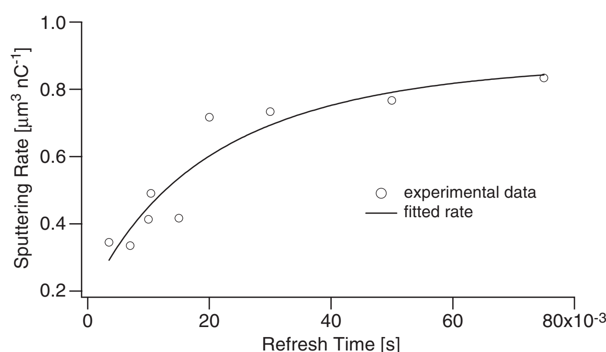

Figure 7. Sputtering rate R of Ti in the presence of XeF_2 as a function of refresh time t_r. Ion current $I_i = 10$ pA and dwell time $t_d = 500$ ns are constant and the gas flow is 1.3×10^{20} molecules cm^{-2} s^{-1}. The full line results from a fit using equation (15) with X_f, k_f, Z_f, and S_f as parameters.

4.3. Theoretical calculations

The sputtering rate may be split into a physical R_p, due to momentum transfer with subsequent sputtering, named sputtering below, and chemical enhanced rate R_{ch}, according to equation (5):

$$R = R_p + R_{ch}. \tag{5}$$

In previous work the physical sputtering R_p was assumed to be independent of the number of adsorbed precursor molecules [23], which we also adopted for this work, setting R_p constant (equation (5)). The yield of the ion induced reaction is linearly dependent on the surface coverage θ according to

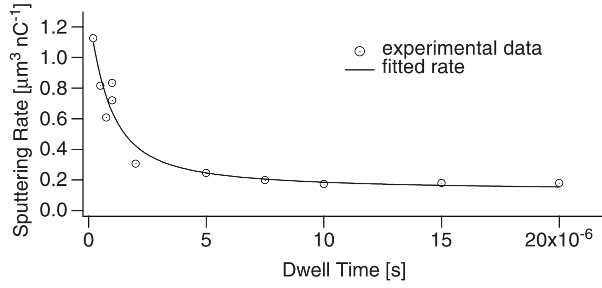

Figure 8. Sputtering rate R of Ti in the presence of XeF_2 as a function of dwell time t_d. Ion current $I_i = 10$ pA and refresh time $t_r = 150$ ms are constant. The XeF_2 flow is 1.3×10^{20} molecules cm^{-2} s^{-1}. The full line is a fit using equation (16). The fit parameters are X_d, k_d, and S_d. Z_d has been calculated using equation (14b).

equation (6),

$$Y_{ch} = q\frac{N(t)}{N_0} = q\theta(t) \tag{6}$$

where N_0 and q represent the density of adsorption sites and an arbitrary factor, respectively. The change in surface coverage is given by equation (7) [23]:

$$\dot{\theta}(t) = \underbrace{\frac{gF}{N_0}(1-\theta(t))}_{\text{adsorption}} - \underbrace{\frac{1}{\tau_{des}}\theta(t)}_{\text{desorption}} - \underbrace{\frac{msJ(t)}{N_0}\theta(t)}_{\text{ion induced reaction}} \tag{7}$$

F is the precursor gas flow; g is the sticking probability; m is the number of precursor molecules participating in a reaction; s is the reaction yield; $J(t)$ is the ion current density; τ_{des} is the spontaneous thermal desorption.

The general solution of this differential equation has the form

$$\theta(t) = Ce^{-kt} + B. \tag{8}$$

For depletion with constant beam current I_i k_d and B_d may be written as

$$k_d = \frac{gF}{N_0} + \frac{1}{\tau_{des}} + \frac{msJ}{N_0} \tag{9a}$$

$$B_d = \frac{gF}{N_0 k_d}. \tag{9b}$$

During the filling period in the absence of current I_i k_f and B_f are

$$k_f = \frac{gF}{N_0} + \frac{1}{\tau_{des}} \tag{10a}$$

$$B_f = \frac{gF}{N_0 k_f}. \tag{10b}$$

The periodic steady-state conditions are defined as

$$\theta_d(0) = \theta_f(t_r) \qquad \text{and} \qquad \theta_f(0) = \theta_d(t_d). \tag{11}$$

Applying the periodic conditions leads to

$$C_d = (B_f - B_d)\frac{e^{-k_f t_r} - 1}{e^{-k_f t_r}e^{-k_d t_d} - 1}. \tag{12}$$

The yield may be calculated introducing the solution (equation (8)) and the periodic steady-state conditions (equation (12)) into equation (6) with subsequent integration over t_d, which results in a rate R_{ch} given by equation (13):

$$R_{ch} = \frac{q}{t_d}\int_0^{t_d}(\theta_d(t) + B_d)\,dt$$
$$= \frac{q\,(B_f - B_d)}{t_d k_d}\frac{\left(e^{-k_f t_r} - 1\right)\left(1 - e^{-k_d t_d}\right)}{e^{-k_d t_d}e^{-k_f t_r} - 1} + qB_d. \tag{13}$$

Z_f and Z_d are linked by equations (14a) and (14b):

$$Z_f = k_d t_d \tag{14a}$$

and

$$Z_d = k_f t_r. \tag{14b}$$

In order to fit the data shown in figure 7 equation (13) has been modified. Since t_d is constant the $k_d t_d$ may be replaced by Z_f, $q(B_f - B_d)$ by X_f, and the integration constant qB_d by S_f.

$$R_f = \frac{X_f}{Z_f}\frac{\left(e^{-k_f t_r}-1\right)\left(1 - e^{-Z_f}\right)}{e^{-Z_f}e^{-k_f t_r}-1} + S_f. \tag{15}$$

Holding t_d constant and varying t_r leads to different surface coverages and consequently a variation of the chemical etch rate (equation (6)). The experimental data shown in figure 7 have been obtained by milling a square of 1 μm length and 500 nm width, as mentioned before. The minimal t_r is determined by the time of a single scan. In order to obtain a further point with shorter t_r, the first point in figure 7 has been obtained by milling a square structure of 500 nm side length.

In a second step the data displayed in figure 8 were fitted using equation (16) holding t_r, thus Z_d, constant. Z_d has been obtained from the parameters of the previous fit using equation (14b).

$$R_d = \frac{X_d}{k_d t_d}\frac{\left(e^{-Z_d}-1\right)\left(1 - e^{-k_d t_d}\right)}{e^{-Z_d}e^{-k_d t_d}-1} + S_d. \tag{16}$$

Holding t_r constant and varying t_d leads again to different surface coverage and thus a variation of the chemical etch rate.

The obtained fit coefficients together with the time constants $\tau = k^{-1}$ for the depletion and filling period are listed in table 1. Z_f was calculated using the parameters determined by the filling experiments (equation (14a)) and compared with the value obtained by the depletion experiments. The calculated and fitted Z_f are in good agreement (table 1). The calculated time constants reveal that adsorption is slow compared to the surface depletion in the presence of the ion current. Consequently, t_d should be as short and t_r as long as possible. We concluded based on our measurements and calculations that optimal conditions for chemical enhanced milling for Ti using XeF_2 are a refresh time t_r longer than 30 ms and a dwell time t_d shorter than 500 ns. For $t_d \to \infty$ the sputtering rate R_d tends to $R = 0.12$ μm^3 nC^{-1}, which corresponds to the physical sputtering rate. For $t_r \to \infty$ the sputtering rate tends to the maximal sputtering rate $R = 0.88$ μm^3 nC^{-1}, which is slightly higher than the value presented above.

Furthermore, chemical etching and physical sputtering yield per ion n can be estimated using equation (17):

$$n = R\frac{\rho}{M_A}N_A e \tag{17}$$

Table 1. Fitting coefficients.

	Filling experiments $t_d = 500$ ns	Depletion experiments $t_r = 150$ ms	
X	1.1	1.2	
Z	0.95[a]	5.1	4.95[b]
S	0.17	0.12	
k_f	33 s^{-1}		
k_d		$1.9 \times 10^6\ s^{-1}$	
$\tau_d = k_d^{-1}$			500 ns
$\tau_f = k_f^{-1}$			30 ms

[a] Z_d has been calculated using $Z_f = k_d t_d$ (equation (14*a*)) and $t_d = 500$ ns used in the experiments.
[b] Calculated value $Z_d = k_f t_r$ (equation (14*b*)) and $t_r = 150$ ms used in the experiments.

n is the yield per ion; $\rho = 4.5$ g cm^{-3} is the density of Ti; $M_A = 47.9$ g mol^{-1} is the atomic weight of Ti; e is the elementary charge.

We assume that the chemical etching and physical sputtering yield per ion n may be expressed as $n = s + p$ (equation (5)), where p represents the contribution of physical sputtering. Applying this condition leads to $p = 1$ and $s = 7$, which means that 1 Ga^+ removes seven Ti atoms with the help of XeF_2. The value of s is rather small compared to literature values of the Si/XeF_2 system [23, 37]. Finally, N_0 is estimated using equations (9*a*) and (10*a*):

$$N_0 = \frac{msJ}{k_d - k_f} \tag{18}$$

where $m = 2$, assuming the chemical enhancement obeying the overall reaction (1):

$$2XeF_2 + Ti \xrightarrow{\text{ion induced}} TiF_4 + 2Xe. \tag{1}$$

With $J = 9$ A cm^{-2} or 5.6×10^{19} ions s^{-1} cm^{-2} we obtain $N_0 = 4.1 \times 10^{14}$ sites cm^{-2}. The surface density n_s of Ti may be estimated according to equation (19):

$$n_s = \left(\frac{\rho}{M_A} N_A\right)^{2/3}. \tag{19}$$

The theoretical value $n_s = 1.5 \times 10^{15}$ molecules cm^{-2} is approximately four times larger than the number of active sites, which means that only 25% of the Ti on the surface acts as adsorption sites.

The presented model considerations do not take into account surface diffusion; nevertheless, reasonable values for refresh and dwell times are obtained.

4.4. Electrical measurements

Figure 9 shows a V–I diagram for a two-point electrical measurement from one contact pad to the other prior to covering the electrodes with a protective SiO_2 layer. A resistance of $R_{pp} > 1$ GΩ has been measured. Measurements after SiO_2 imbedding of the electrodes have not shown a significant difference of the resistance R_{pp}. A complete electrical characterization of the electrode array is out of the scope of this work, but further work should be done concerning this subject.

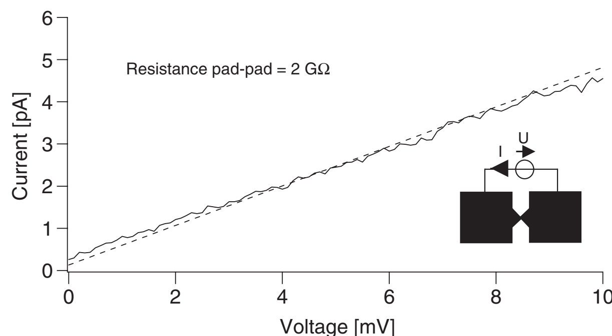

Figure 9. V–I diagram recorded over the pads of the 50 nm interdigitated electrodes. The resulting resistance R is ~2 GΩ determined from the slope of the current curve.

5. Conclusion

We fabricated interdigitated Ti electrode arrays with a 50 nm width and a 50 nm gap, which are embedded in SiO_2 using the FIB technique. In order to achieve high quality nanostructures, the removal process has been chemically enhanced using XeF_2, which leads to an increase of the etching rate by a factor of seven. Furthermore, gas assisted etching leads to a reduction of redeposition, which significantly increases the quality of the milled structures. In order to optimize the adsorption limited etch process the etch rate has been maximized, varying refresh time t_r and dwell time t_d, and appropriate t_d and t_r have been determined. In addition, the measured values have been reproduced using a simple adsorption–desorption model. The numerically determined and the measured values are in good agreement. The time constants for the dwell t_d and refresh time t_r are $\tau_d = 500$ ns and $\tau_f = 30$ ms, respectively. V–I measurements revealed that the resistance of the electrode array is higher than 1 GΩ, which is therefore sufficiently high for a wide range of applications.

Acknowledgments

The authors gratefully acknowledge TOP NANO 21 for financially supporting this work and CMI (Centre of MicroNanotechnology of École Polytechnique Fédérale de Lausanne) for the technical support. The authors also thank N Xanthopoulos for carrying out the XPS measurements.

References

[1] Li J *et al* 2001 *Nature* **412** 166
[2] Arrigan D W M 2004 *Analyst* **129** 1157
[3] Koehne J *et al* 2004 *J. Mater. Chem.* **14** 676
[4] Li J *et al* 2003 *Nano Lett.* **3** 597
[5] Shahidi G G, Antoniadis D A and Smith H I 1989 *IEEE Trans. Electron Devices* **36** 2605
[6] Montelius L, Tegenfeldt J O and Ling T G I 1995 *J. Vac. Sci. Technol.* A **13** 1755
[7] Finot E *et al* 2003 *Ultramicroscopy* **97** 441
[8] Laureyn W, Van Gerwen P, Suls J, Jacobs P and Maes G 2001 *Electroanalysis* **13** 204
[9] Toohey M J 2005 *Sensors Actuators* B **105** 232
[10] Diguet R, Pralat K and Jadzyn J 1982 *Chem. Phys. Lett.* **90** 391
[11] Nagase T, Gamo K, Kubota T and Mashiko S 2005 *Microelectron. Eng.* **78/79** 253

[12] Zandbergen H W *et al* 2005 *Nano Lett.* **5** 549
[13] Montelius L *et al* 2000 *Microelectron. Eng.* **53** 521
[14] Schift H, Jaszewski R W, David C and Gobrecht J 1999 *Microelectron. Eng.* **46** 121
[15] Van Gerwen P *et al* 2000 *J. Micromech. Microeng.* **10** N1
[16] Russell P E, Stark T J, Griffis D P, Phillips J R and Jarausch K F 1998 *J. Vac. Sci. Technol.* B **16** 2494
[17] Casey J D, Doyle A F, Lee R G, Stewart D K and Zimmermann H 1994 *Microelectron. Eng.* **24** 43
[18] Ochiai Y *et al* 1985 *Japan. J. Appl. Phys.* 2 **24** L169
[19] Taniguchi J, Ohno N, Takeda S, Miyamoto I and Komuro M 1998 *J. Vac. Sci. Technol.* B **16** 2506
[20] De Marco A J and Melngailis J 2005 personal communication
[21] Gandhi A and Orloff J 1990 *J. Vac. Sci. Technol.* B **8** 1814
[22] Harriott L R 1993 *J. Vac. Sci. Technol.* B **11** 2012
[23] Edinger K and Kraus T 2000 *J. Vac. Sci. Technol.* B **18** 3190
[24] Edinger K and Kraus T 2001 *Microelectron. Eng.* **57/8** 263
[25] Chen X *et al* 2003 *Mater. Sci. Eng.* A **352** 221
[26] Matsui S *et al* 2000 *J. Vac. Sci. Technol.* B **18** 3181
[27] Reuter D, Werner C, Wieck A D and Petrosyan S 2005 *Appl. Phys. Lett.* **86** (April)
[28] Melngailis J 1993 *Nucl. Instrum. Methods Phys. Res.* B **81** 1271
[29] Reyntjens S and Puers R 2001 *J. Micromech. Microeng.* **11** 287
[30] Daniel J H, Moore D F and Walker J F 2000 *Smart Mater. Struct.* **9** 284
[31] Giannuzzi L A and Stevie F A 2005 *Introduction to Focused Ion Beam* (Berlin: Springer) p 357
[32] Reyntjens S 2005 personal communication
[33] Coburn J W and Winters H F 1979 *J. Appl. Phys.* **50** 3189
[34] Friedli V 2006 personal communication
[35] Tseng A A, Insua I A, Park J S, Li B and Vakanas G P 2004 *J. Vac. Sci. Technol.* B **22** 82
[36] Orloff J, Utlaut M and Swanson L 2003 *High Resolution Focused Ion Beams: FIB and Its Applications* (New York: Dordrecht, Kluwer Academic) p 303
[37] Young R J, Cleaver J R A and Ahmed H 1993 *J. Vac. Sci. Technol.* B **11** 234